Review

Basics of Modern Photogrammetry

Mathias J.P.M. Lemmens *

Posted Date: 18 March 2026

doi: 10.20944/preprints202603.1489.v1

Keywords: digital photogrammetry; image matching; structure from motion; semi-global matching; camera model; camera calibration; feature extraction; georeferencing; digital elevation model; accuracy assessment

Preprints.org (www.preprints.org) | NOT PEER-REVIEWED | Posted: 18 March 2026 doi:10.20944/preprints202603.1489.v1

Review

Basics of Modern Photogrammetry

Mathias J.P.M. Lemmens

Independent Researcher, Delft, Netherlands; mlemmens@geotexs.nl

Abstract

Digital photogrammetry emerged around 1980 and decisively accelerated the automation of workflows for converting images into georeferenced datasets for a wide range of applications. The development of innovative technologies, including metric digital cameras; the miniaturization of powerful computers; and positioning and orientation systems, has accelerated since the turn of the century. Advanced photogrammetric and computer vision algorithms have been developed and implemented in software, allowing many workflows to run on computers from begin to end. Today, final products can be generated largely automatically, minimizing the timespan between image capture, even up to real-time, and acquiring the necessary datasets for the task at hand,. Thanks to the wide availability of commercial and open-source software, the scope of applications has expanded rapidly, leading to a significant growth in the number of new users of photogrammetry. This article aims to serve this new group by providing an overview of the technologies underlying current photogrammetric workflows, starting with the geometric fundamentals of camera modeling and georeferencing. Next, we examine the algorithms that have revolutionized workflows and are known by various names, particularly: image matching, computer stereo vision, and structure from motion (SFM). Next basic characteristics of final photogrammetric products are briefly discussed. This is followed by methods to assess accuracy of the final product, a key component of extracting geometric information from imagery. The discussion section provides tips for selecting suitable textbooks to deepen your knowledge.

Keywords: digital photogrammetry; image matching; structure from motion; semi-global matching; camera model; camera calibration; feature extraction; georeferencing; digital elevation model; accuracy assessment

1. Introduction

Photogrammetry is an advanced measurement technique that originated over 150 years ago. Throughout its long history, the fundamental geometric principles have essentially remained unchanged. Manually extracting geometric information from images is labour-intensive and computationally tough. Therefore, the main research efforts have focused on reducing human involvement in converting 2D (x,y) coordinates of image points into 3D (X,Y,Z) coordinates of points of interest in an object-space-based coordinate system, such as a National Geodetic Reference System or WGS84. The complexity proved so enormous that photogrammetry developed into an autonomous discipline with its own scientific and professional organizations. Modern photogrammetry builds on digital photogrammetry research that began around 1980. Around the year 2000, these efforts culminated in significant changes in photogrammetric workflows documented in [1–3]. Since 2000, intensive research into further automation rapidly increased, resulting in many photogrammetric tasks and processes now being implemented in a wide range of user-friendly software packages. Many new applications emerged and continue to emerge, accompanied by a significant increase in specialists at the application side, for whom photogrammetry is proving to be an advantageous and expedient measurement technique. Key developments include:

- Digital metric camera's aimed at accurate (topographic) mapping and 3D object modeling;

doi:10.20944/preprints202603.1489.v1

- Affordable, powerful computers; large storage space and high-speed internet;
- Miniaturization of integrated GNSS-receivers and IMU-systems – called Position and Orientation Systems (POS);
- Unmanned Airborne Systems (UAS) – often called drones;
- New geodata product: 3D point clouds, created from overlapping imagery by image matching as well as directly acquired from Lidar through laser scanning;
- Oblique cameras enabling the (semi-)automatic generation of digital 3D landscapes and city models – often called digital twins.

The cross-fertilization between photogrammetry and 3D computer vision has been a major driving force for automated image matching, in 3D computer vision known as Structure from Motion (SfM), for detecting corresponding points in overlapping images. Today, the extraction of X,Y,Z-coordinates from images is done entirely digitally using fast computers, petabytes of storage and commercial or open source software, minimizing the time span between image acquisition and final photogrammetric products. Today's (semi)automatic processes turn photogrammetry into a seemingly straightforward task.

This paper aims at serving users of photogrammetry stemming from application sides, including GIS analysts, through providing the basic concepts of automatically extracting X,Y,Z-coordinates from overlapping digital images. For brevity's sake the outlining will focus on images captured from airborne platforms. However, the principles are equally valid for ground based platforms such as cars and trolleys.

2. From Camera Coordinates to 3D Object Coordinates

2.1. Orthogonal Versus Central Projection

Although an aerial image resembles a map, the types of projection of these two planar representations significantly differ. The projection of a map is orthogonal – there is only a scale difference between mapped area and map (Figure 1a). Calculation of the distance in object space just requires multiplication of the measured map distance with the scale factor (S). In an image, this property only occurs in the rare case where the image plane is exactly parallel to the terrain and the terrain is flat. In all other cases, scale differences occur. Nevertheless, the term image scale is often used. This is a nominal scale defined by the focal length of the camera divided by the mean distance to the object, in aerial images this is the flight height.

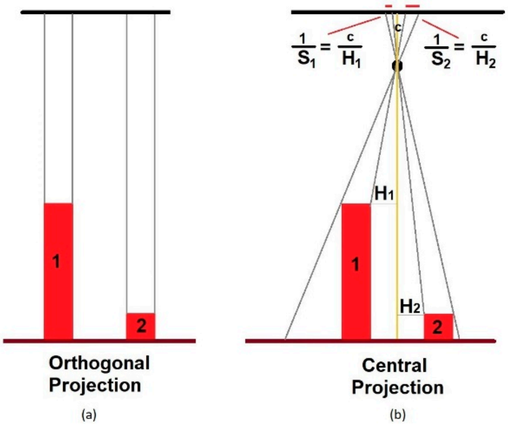

Orthogonal Projection
(a)

Central Projection
(b)

Figure 1. (a) Orthogonal (map) projection, (b) Central projection; S_1 and S_2 denote scale factors and H_1 and H_2 the objects distances to the projection center.

2.2. Geometric Camera Model

The central projection established by the camera lens system ensures that the rays of sunlight reflected by the scene pass the camera exactly through one point, called projection center (Figure 1b). Next the ray of light meets the image plane and leaves its mark there. The intensity of the ray, which depends on the reflection properties of the object and the scattering and absorption properties of the atmosphere, determines whether the image spot is dark, bright or somewhere in between. The fundamental notion is that object point, projection center and image point constitute one straight line; they are collinear. Consequently each and every point in the image uniquely correspondents to one point in object space.

The optical axis perpendicularly intersects the image plane at the principle point (x_0,y_0) which usually slightly deviates from the origin of the image (Figure 2a). The distance of the projection center to the image plane – calibrated focal length (c) – and the position of the principle point with respect to the image origine are the interior orientation parameters (x_0,y_0,c), which have to be known with micrometer precision requiring careful calibration. The smaller the focal length the larger the field of view (FoV) and thus the larger the area captured (Figure 3a). This is economically advantageous but causes excessive lean over (relief displacement) and occlusion (Figure 3b,c).

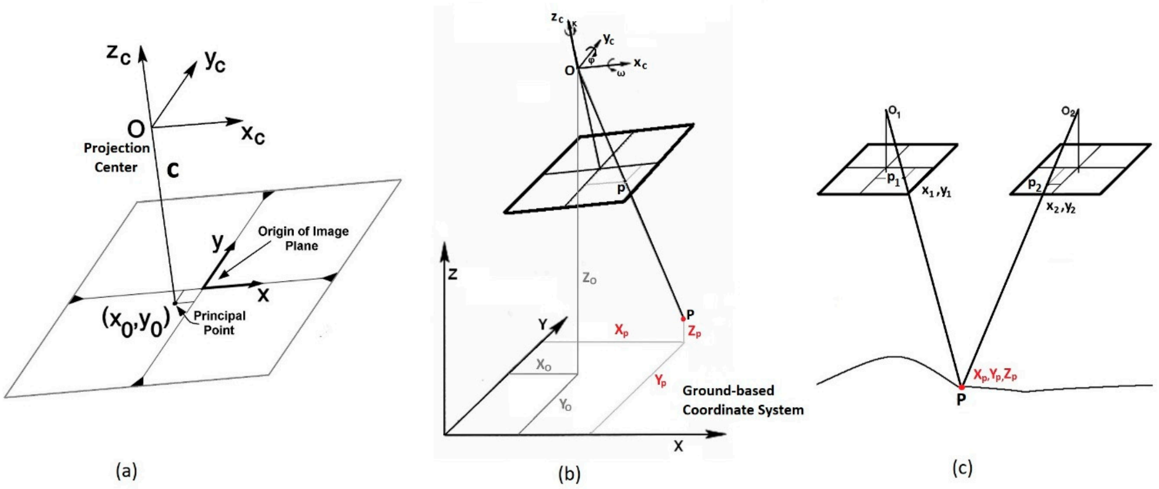

Figure 2. (a) (x_0,y_0,c) are the interior orientation parameters of the camera; x_c, y_c and z_c indicate the axes of the camera coordinate system, (b) Tying the camera coordinate system the the ground-based coordinate system through the six exterior orientation parameters: three coordinates of the projection center (O): X_0,Y_0,Z_0 and three orientation parameters ω, ϕ and κ, (c) If the three interior orientation parameters and the six exterior orientation parameters are known 3D-coordinates of points in object space (X_P,Y_P,Z_P) can be computed from at least two overlapping images; x_1,y_1 are the coordinates of point P in the one image and x_2,y_2 the coordinates in the second image.

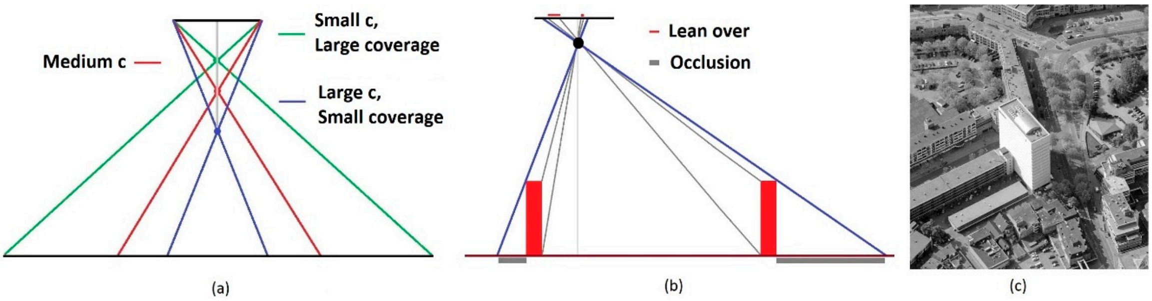

Figure 3. (a) Relationship between focal length and field of view (FoV), (b) Wide area aerial camera (small focal length) causses excessive lean over and occlusion of buildings and other high objects, (c) Lean over and occlusion demonstrated by an oblique Pictometry image (sources: (a),(b) [5] (p. 71); (c) [4]).

doi:10.20944/preprints202603.1489.v1

2.3. Collinearity Equation

The fundamental notion that object point, projection center and image point constitute one straight line is the starting point for computing 3D object space coordinates from camera coordinates. Essential is that the object space coordinates of the projection center at the instant of exposure (X_0, Y_0, Z_0) are known as well as the three angles (ω, ϕ, and κ; omega, phi, kappa) of the direction of the optical axis and thus the orientation of the image plane with respect to the three axes of the object space reference system (Figure 2b). The 6 parameters (X_0, Y_0, Z_0) and (ω, ϕ, κ) are the exterior orientation parameters. The direction of the optical axis is described by sinus and cosine functions of ω, ϕ, and κ, in total they are nine: three for each axis of the object space coordinate system. The rotation is given by a 3×3-matrix, containing the elements r_{ij}, i=1,...,3; j=1,...,3. The mathematical relationship of the camera coordinates (x,y,c), the exterior orientation parameters (X_0, Y_0, Z_0; ω, ϕ, κ), and the (X,Y,Z) coordinates of the corresponding object space point can be derived from projective geometry after many straightforward steps resulting in the collinearity equation:

$$\begin{aligned} x - x_0 &= -c\,\frac{r_{11}(X - X_0) + r_{21}(Y - Y_0) + r_{31}(Z - Z_0)}{r_{13}(X - X_0) + r_{23}(Y - Y_0) + r_{33}(Z - Z_0)} \\ y - y_0 &= -c\,\frac{r_{12}(X - X_0) + r_{22}(Y - Y_0) + r_{32}(Z - Z_0)}{r_{13}(X - X_0) + r_{23}(Y - Y_0) + r_{33}(Z - Z_0)} \end{aligned} \tag{1}$$

From measuring two image coordinates (x,y) of a point the three (X,Y,Z) coordinates of the corresponding point in object space can't be calculated, since it is impossible to calculate three unknowns from two observations. A second image is required showing the same part of object space from another viewpoint. With four image coordinates the three object space coordinates can be computed. This second image provides also a straight line and its spatial intersection with the straight line of the first image, results in a unique solution (Figure 2c).

2.4. Georeferencing

To utilize the collinearity equation the parameters of interior and exterior orientations of each image have to be known. The first are determined by calibration while X_0, Y_0, Z_0; ω, ϕ, κ are determined either directly during survey, indirectly or by a combination of both. Direct measurement relies on the use of onboard GNSS and IMU. GNSS provides the position coordinates of the projection center at the instant of exposure and IMU the three angles of orientation of the image plane. In a Positioning and Orientation System (POS) GNSS-receiver and IMU are integrated. Indirect determination is done by using Ground Control Points (GCP). Whatever method is used, geo-referencing starts with the relative orientation of the images also called registration or co-registration, which requires the determination of corresponding points in the overlaps. These tie or key points may be few but must be well-distributed over the overlaps (Figure 4). To obtain high precision the image coordinates of tie points must be determined at subpixel level using Least Squares Image Matching (LSM). Next the co-registered coordinates are transformed to a ground-based reference system. This step requires either the POS-output or X,Y,Z coordinates of GCPs or a combination of both. The two-step procedure of relative and absolute orientation can be conducted in one single step by incorporating the image coordinates of tie-points, the interior orientation parameters, the approximate values of exterior orientation parameters, which are obtained from onboard POS-measurements, and ground-based coordinates of GCPs in one rigorous least squares adjustment process.

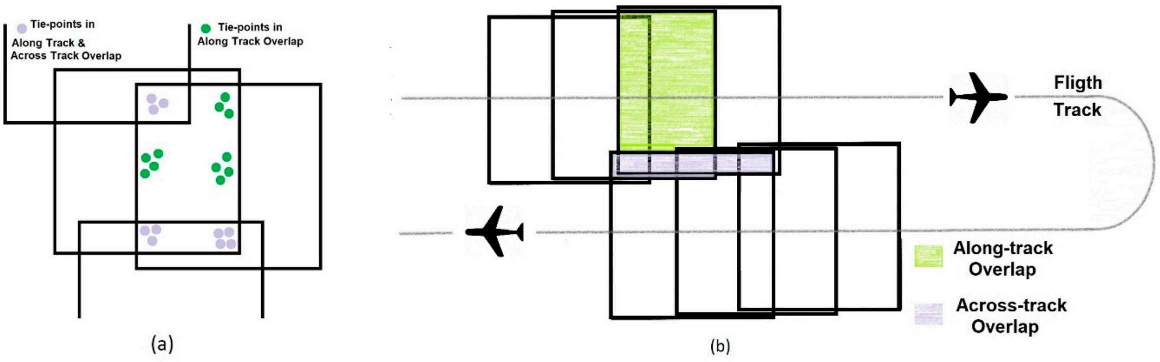

Figure 4. (a) Distribution of tie points in the along-track and across-track overlaps, (b) Shown for the conventional overlaps in aerial photogrammetry: 60% along-track overlap, 20% across-track overlap (source: [5] (pp. 66, 77)).

2.5. Deviations from the Ideal Camera Model

2.5.1. Modelling Deviations

A camera is a mechanical, opto-electronic construction, which operates in a physical, sometimes harsh, environment. So, (slight) deviations from the theoretical camera model easily occur in practice. For precision application the deviations have to be modelled and described mathematically. Major deviations are radial lens distortions and irregularities in the image plane, including non-square shape of pixels and different scaling factors for rows and columns. A review of camera deviations is provided in [6].

2.5.2. Calibration with Network of Known Points

High precision applications require accurate calibration of interior orientation parameters under well-conditioned laboratory conditions – e.g. annually – using a network of known points ensembled in a frame. Although heavyweight metric cameras are exceptionally stable, their interior orientation parameters may deteriorate over time. A solution is to capture a network of known points immediately before and after the survey.

2.5.3. Self-Calibration

Metric cameras are bulky, heavy and expensive. Lightweight, non-metric cameras and consumer-grade cameras are increasingly preferred for conducting surveys using as platforms UASs, cars, human backs and so. The elements of interior orientation of non-metric cameras may change during survey. Hence, calibration at forehand is inappropriate. Since the interior orientation parameters have to be determined separately for each image, direct in-survey calibration is required. This so-called self-calibration can be done through mathematical extension of the collinearity equation (Equation 1) provided that the images have sufficient overlap. The direct computation of the interior orientation parameters allows the gathering of precise coordinates from non-metric cameras and even consumer-grade cameras. In addition along with miniaturization of electronics, POS and lightweight materials, self-calibration has given a boost to the popularity of (UAS) photogrammetry. The mathematical concepts of camera self-calibration are elaborated in [7].

3. Image Matching / Structure from Motion

Now we come to the core of modern photogrammetry: image matching, also called Structure from Motion (SfM), which is essential for the automatic processing of images. Image matching aims to automatically trace corresponding points in overlaps for three main goals: (1) detecting tie points in the (co-)registration step of the workflow; (2) generating dense point clouds, e.g., DEMs; and (3) creating 3D models of power lines, cultural heritage sites, quarries, cities and many other objects. The many methods that have been developed over time can be divided into two main groups: (1) area-based methods and (2) feature-based methods [8]. The intensive research into both groups since the 1980s has yielded a wide range of algorithms, driven by the many appearances of stereo images, object spaces, and the tasks at hand. Notably are:

- Required accuracy;
- Required point density;
- Tie point detection for (co-)registration requires high robustness, reliability and precision;
- Image content – presence of contrast, texture and distinctive points;
- Illumination differences between overlapping images;
- Perspective differences, creating non-parallel, rotated images with scale differences;
- Computational and storage demands.

Area-based methods model images as a 2D spatial discrete distribution of grey values. In feature-based methods images are approached as a set of L-shaped corners, T- and other types of junctions, edges, blobs and other feature types.

3.1. Area-Based Matching

3.1.1. Normalized Cross-Correlation (NCC)

Initially area-based matching explored correlation methods, using similarity measures on the grey values in regularly shaped patches in the overlap. Particularly the normalized cross correlation coefficient (R) of two image patches has been explored. A R-value close to 1 indicates good similarity, around 0 no or little similarity and when R reaches -1 (minus one) the correlation is negative. R is a function of the covariance of the grey values in the two images patches and the standard deviations of each patch. The target patch is shifted pixel by pixel over the search patch resulting in a discrete cross-correlation function. If R_{max} exceeds a predefined threshold (R_t) the pixel is marked as potential corresponding point. Figure 5 illustrates the principle and shows the equation to compute R. In patches with little texture or no features the discrete cross-correlation function yields everywhere over the search patch the same high value, so that the potential corresponding point has to rejected. To avoid wasting of computation time the target patch should contain a distinctive point to be detect by an interest operator prior to conducting NCC-computation. Cross correlation can cope with a linear transformation in grey values but not with geometric differences between the overlaps, while these often have different orientations and scales.

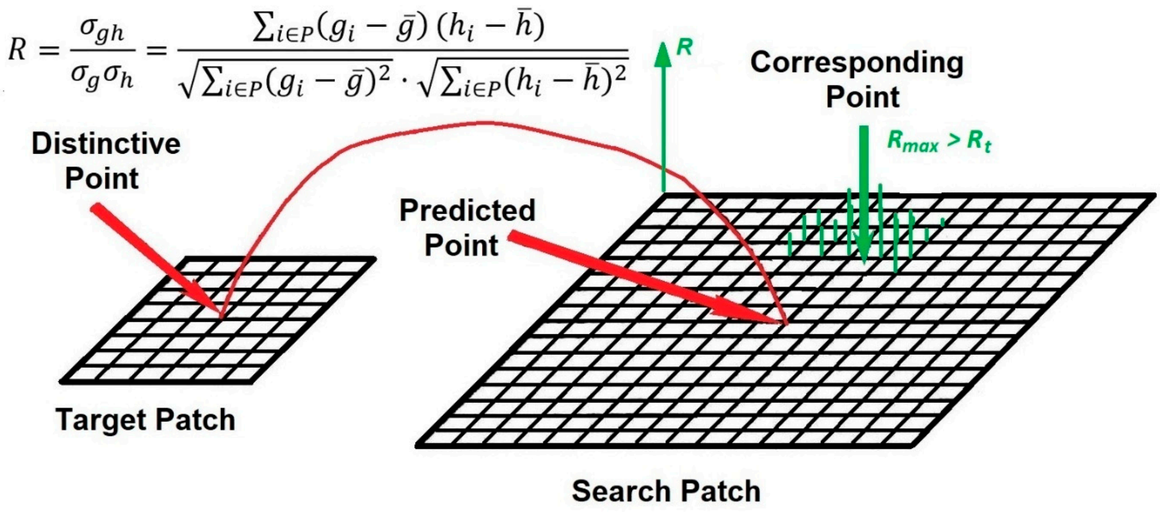

Figure 5. Area-based matching using NCC; after detection of a distinctive point in the target patch the location of the corresponding point in the search patch is predicted and determined by shifting pixel by pixel the target

patch over the search patch to compute the NCC-function. If R_{max} exceeds a predefined maximum R_t the pixel is preliminary marked as corresponding point and further scrutinized on reliability of the correspondence.

3.1.2. Least Squares Image Matching (LSM)

Photogrammetrists found a solution to the differences in geometry between overlaps by explicitly modelling them. To maintain the advantageous property that cross-correlation can cope with a linear transformation in grey values this transformation is also modelled. The mathematical modelling is solved through least squares adjustment [9–11]. Although computational demanding (LSM) results in high subpixel accuracy, even up to 1% of a pixel. LSM is therefore the preferred final matching step for tie point determination for high definition photogrammetric applications. LSM models the geometric and grey value differences between a point in the target patch **g** with image coordinates (x_t,y_t) and the unknown corresponding point (x_s,y_s) in the search patch **h** by:

$$\boldsymbol{g}(x_t, y_t) = \boldsymbol{A}\big(\boldsymbol{h}(x_s, y_s)\big) \tag{2}$$

where **A**(·) denotes the non-linear relationship. The grey value differences are usually modelled by a linear relationship and the geometric differences as an affine transformation, which is expressed in parametric form as a first order polynomial with six unknowns. Accordingly Equation 2 becomes:

$$g(x_t, y_t) = r_1 h(p_1 + p_3 x_t + p_4 y_t, p_2 + p_5 x_t + p_6 y_t) + r_0 \tag{3}$$

Since Equation (3) is non-linear the expression has to be expanded in a Taylor series around approximate values of the eight unknowns: (r_1,r_2) and (p_1,…,p_6). The equation is solved by using 5x5 patches, 7x7 patches or larger, resulting in an overdetermined system of equations, which is iteratively solved by non-linear Least Squares Adjustment (LSA). This procedure requires approximate image coordinates of the corresponding point with a precision of a few pixels. Therefore, LSM is particularly suited to find sub-pixel location of the corresponding point once a (rough) match has been found by an earlier, less computational demanding method.

3.2. Feature-Based Image Matching (FBM)

FBM detects distinctive points in both target and search image, and assigns feature measures to them computed from a patch of grey values. Next, each distinctive point in the target patch is linked to the point in the search patch with the most similar feature values. The size of the image patches have to be predefined. For obtaining reliable matches the distinctive points should be located at T-junctions, corners, blobs and the like features (Figure 6a). Edges do not belong to these features, because correspondence can be found along many places of the boundary (Figure 6b).

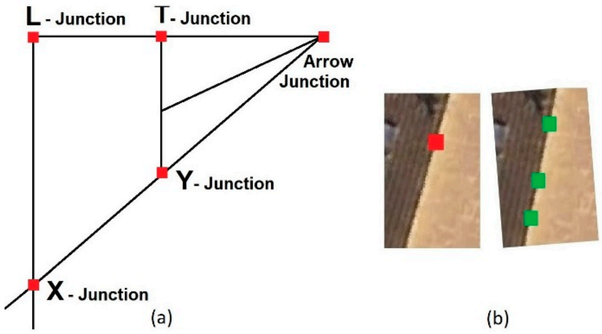

Figure 6. (a) L-junctions, Y-junctions, T-junctions, Arrow-junctions, and X-junctions are important distinctive points for area-based and feature-based matching (source: [5] (p. 252)), (b) When using 2D image patches to trace corresponding points, edges are unsuited for matching; the corresponding point (green) in the search patch of the point in the target image (red) can lie all along the edge (source: [5] (p. 257)).

Distinctive point detectors are called interest operators, key point operators, salient point detectors, significant point detectors or corner detectors. A variety of interest operators have been

doi:10.20944/preprints202603.1489.v1

developed. Basically, they compute first or second derivatives. Since differentiation amplifies noise they are usually combined with a Gaussian smoothing kernel, which is derived from the 2D Gaussian function. A widely used interest operator based on first derivatives is the Förstner-Harris Operator while the Dreschler-Nagel operator is based on computing second derivates. Both approaches are insensitive to mutual rotation of the overlapping images, but not to scale differences. To cope with scale differences Lowe developed an empirical approach, called Scale Invariant Feature Transform (SIFT), in which distinctive points are detected by interest operators of different sizes based on the Laplacian of Gaussian (LoG) [12,13]. These three operators are treated below.

3.2.1. Förstner-Harris Operator

Calculation of features is based on two principles. The distribution of grey values over 2D space is either considered from a statistical view point or is treated as a curved 2D surface in 3D space. In the statistical view the eigenvalues of the 2x2 covariance matrix of the grey values in image patches are computed. Since we are not interested in the location of the origin of the eigenspace nor in the absolute size of the eigenvectors, but only in the shape of the eigenspace and the strength of the response, the computation of the covariance matrix can be simplified to:

$$\boldsymbol{C} = \begin{pmatrix} \sum g_x^2 & \sum g_x g_y \\ \sum g_x g_y & \sum g_y^2 \end{pmatrix} \tag{4}$$

With g_x and g_y the gradients over row and column directions computed using two orthogonal differential operators e.g. Prewitt, Sobel or Frei-Chen operator of which the kernels are shown below, with t=1 (Prewitt), t=2 (Sobel) and t=√2 (Frei-Chen):

$$g_x = G * \begin{bmatrix} +1 & 0 & -1 \\ +t & 0 & -t \\ +1 & 0 & -1 \end{bmatrix} \qquad g_y = G * \begin{bmatrix} +1 & +t & +1 \\ 0 & 0 & 0 \\ -1 & -t & -1 \end{bmatrix} \tag{5}$$

The edge strength per pixel, M(i,j), and the direction of the gradient, θ(i,j,) are computed from the two responses according to:

$$M(i,j) = \sqrt{g_x^2(i,j) + g_y^2(i,j)}\ ; \qquad \theta(i,j) = \text{atan}\frac{g_y(i,j)}{g_x(i,j)} \tag{6}$$

The summation in Equation 5 is carried out over e.g. a 5x5 image patch. The two eigenvalues ($\lambda_{1,2}$) are computed according to:

$$\lambda_{1,2} = \frac{1}{2}\left(\sum g_x^2 + \sum g_y^2\right) \pm \sqrt{\left(\frac{\sum g_x^2 - \sum g_y^2}{2}\right)^2 + \left(\sum g_x g_y\right)^2} \tag{7}$$

A corner or other junction type is suited to act as distinctive point if the values of λ_1 and λ_2 are similar, expressed by the measure q in Equation 8 and both λ_1 and λ_2 exceed a predefined threshold to avoid acceptance of weak distinctive points, expressed by the measure w (Figure 7).

$$q = 1 - \left[\frac{\lambda_1 - \lambda_2}{\lambda_1 + \lambda_2}\right]^2 ; \qquad w = \frac{\lambda_1 \lambda_2}{\lambda_1 + \lambda_2} \tag{8}$$

The values of q range from 0 to 1. If q lies close to 1, a corner or other junction type is present. If q lies close to 0, the operator has detected an edge.

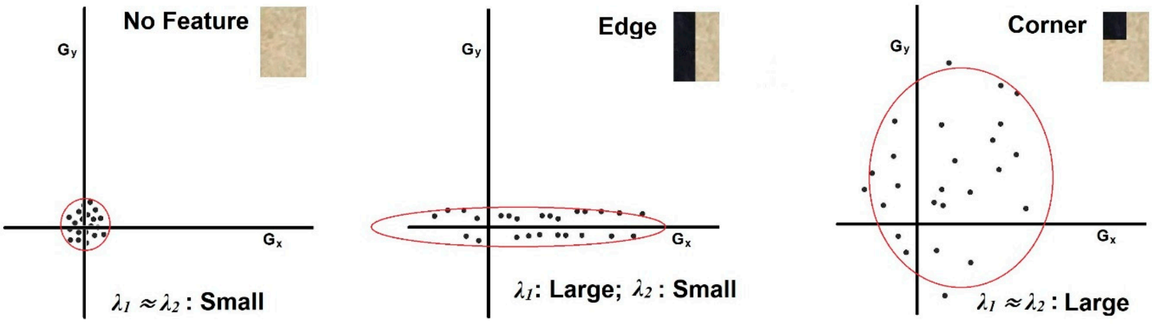

Figure 7. Computation of eigenvalues λ_1 and λ_2 corresponds to fitting an ellipse through the scatter plot of the responses of the two orthogonal differential kernels; the size of λ_1 and λ_2 determines whether no feature is present, an edge, a corner or any other distinctive point shown in Figure 6a (source: [5] (p. 273)).

The above approach has been independently developed in the field of digital photogrammetry [14,15] and in computer vision [16] more or less at the same time. Figure 8a outlines the pipeline of this operator.

3.2.2. Dreschler-Nagel Operator

Dreschler and Nagel looked at grey values as a curved 2D surface in 3D space, which allows to explore the basics of differential geometry in which the Gaussian curvature ($K = k_1 \times k_2$) plays a key role [17,18]. K and the principle curvatures (k_1 and k_2) are invariant to image rotations and are computed from the second derivatives of an image: G_{xx}, G_{yy} and G_{xy}, which are obtained by convolving the image with three kernels:

$$G_{xx} = G * \begin{bmatrix} 1 & -2 & 1 \end{bmatrix} \quad G_{yy} = G * \begin{bmatrix} 1 \\ -2 \\ 1 \end{bmatrix} \quad G_{xy} = G * \begin{bmatrix} 1 & -1 \\ -1 & 1 \end{bmatrix} \tag{9}$$

Now k_1 and k_2 can be determined from an eigenvalue analysis of the Hessian, which is a symmetric matrix:

$$\boldsymbol{H} = \begin{bmatrix} G_{xx} & G_{xy} \\ G_{xy} & G_{yy} \end{bmatrix} \tag{10}$$

k_1 and k_2 are calculated from solving the quadratic form:

$$\kappa^2 - \kappa\left(G_{xx} + G_{yy}\right) + G_{xx}G_{yy} - G_{xy}^2 = 0 \tag{11}$$

With solution:

$$\kappa_{1,2} = \frac{1}{2}\left[G_{xx} + G_{yy} \pm \sqrt{\left(G_{xx} + G_{yy}\right)^2 - 4\left(G_{xx}G_{yy} - G_{xy}^2\right)}\right] \tag{12}$$

- If k_1 and k_2 are both small, only little grey value differences or random texture will be present;
- If k_1 is large and k_2 small, the type of curvature indicates the presence of an edge;
- If $k_1 \approx k_2$ and both are large, the type of curvature indicates the presence of a corner-like junction, blob, and other distinctive points of interest.

Figure 8b outlines the pipeline of this operator.

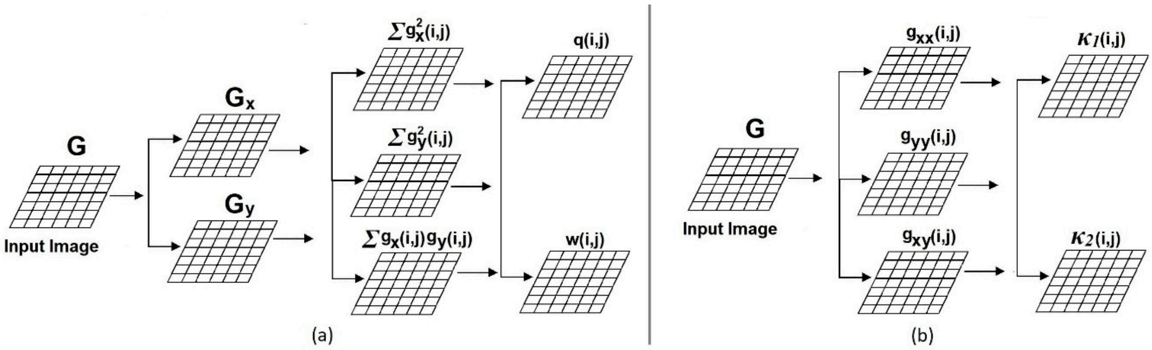

(a) (b)

Figure 8. Diagrams demonstrating the pipelines of (a) Förstner-Harris interest operator (source: [5] (p. 274), (b) Dreschler-Nagel interest operator (source: [5] p. 279)).

3.2.3. Scale Invariant Feature Transform (SIFT)

In contrast to the above interest operators, SIFT can handle scale differences between overlapping images. Operators, which are not scale invariant, are not an issue for images taken with the same camera at similar object distances and parallel to each other. However, increasingly overlapping images are taken from platforms such as UAS and with oblique cameras. Due to scale differences in such images, a corner in one image appears as a curved edge in another (Figure 9).

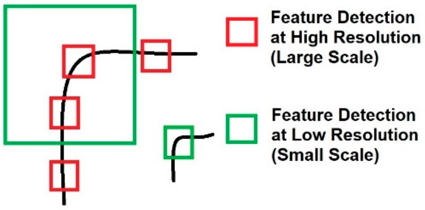

Figure 9. Corner in a high resolution image (large scale) appears as a curved edge in a low resolution image (small scale) (source: [5] p. 276).

Scale Invariant Feature Transform (SIFT) is an empirical approach, developed by David Lowe in which distinctive points are detected by interest operators of different size [13,14]. Transform refers to the conversion of an image into a set of features, which are invariant to shift, rotation and scaling. A rotation invariant operator is the Laplacian-of-Gaussian (LoG) which is implemented in a modified form to save computation time – called Difference-of-Gaussians (DoG) – which subtracts the output of different Gaussian smoothed versions of the image (see Appendix A). The output is a set of candidate interest points – key points – which are further scrutinized to separate edges from distinctive points, the latter being the actual points of interest. Separation is done with the Dreschler-Nagel operator. The explicit time-consuming calculation of the two principle curvatures according to Equation 12 is avoided by introducing an alternative measure:

$$\frac{\left(G_{xx}+G_{yy}\right)^2}{G_{xx}G_{yy}-\left(G_{xy}\right)^2}<\frac{(r+1)^2}{r} \tag{13}$$

With r the ratio between the largest principle curvature and the smallest one, e.g. 10. The point is marked as interest point if the above decision criterion is met. Next the orientations of the gradients are computed, and weighted based on their gradient magnitude, computed according to the left part of Equation 6 and the distance of the concerning pixel to the interest point. The latter is done by a Gaussian decaying weighting. Next the orientations are plotted in a compass card histogram uniformly divided into e.g. 36 segments. The histogram maxima are identified as interest points to which feature descriptors are assigned for finding the corresponding points in other images. This is done by defining a 16 x 16 patch around the interest point containing the weighted orientations and

doi:10.20944/preprints202603.1489.v1

subdividing this patch into sixteen 4 x 4 windows, each window containing 16 pixels. Per 4 x 4 window the orientations are mapped into a compass card subdivided into 8 segments, i.e. each segment covers 45 degrees (Figure 10), resulting in 4 x 4 x 8 orientation segments, which are grouped in a vector of length 128 in a fixed order. Candidate corresponding points whose vectors show the greatest similarity are designated corresponding points.

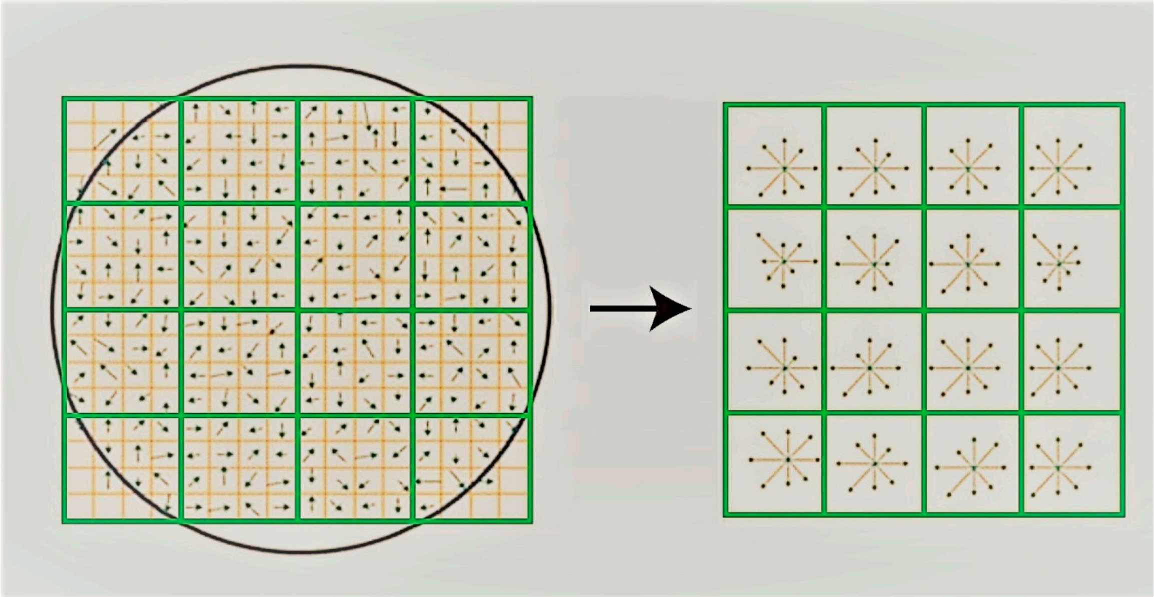

Figure 10. Sketch illustrating the projection of the gradient orientations of the SIFT operator into a compass card whose values get stored in a vector of length 128; the circle outlines the influence sphere of the Gaussian decaying weight function (source: [13]).

SIFT and its modifications are widely applied in FBM applications, including image mosaicking, tie point matching and 3D modeling of objects. The design originates in computational efficiency considerations. The computation of the vector of 128 descriptors is costly, which impedes real-time use for e.g. simultaneous localization and mapping (SLAM) or real-time object tracking. Other researchers developed modifications to enable near real-time computation of matches [19,20]. Other impediments inducing modifications include differences in contrast among multisource images, computational burden of large images, heterogeneous distribution of distinctive points and accuracy issues. The SIFT operator has been patented in 2004.

3.3. Semi-Global Matching (SGM)

The conventional area-based and feature-based matching systems do not find corresponding points – and if they find the match is unreliable – in areas with low contrast/texture. They are prone to error for deserts, dunes, road pavements and roofs, while in the presence of neighboring repetitive patterns wrong matches frequently occur. Such areas have low point density resulting in an inhomogeneous distribution of points, which is unfavorable for many applications. They also fail in the presence of height discontinuities and occlusions. The basic notion to overcome this disadvantage is to implement knowledge on the global shape of the object space as an additional constraint. Global matching simultaneously balances the similarity values between candidate corresponding points and the shape of the surface on which these points lie. For long, practical use of global matching was hampered by exorbitantly high processing time and memory consumption. The rise of programmable graphical processing units (GPU), which increased computer power, stimulated investigations on algorithmic solutions to global matching.

The basic solution explored by Heiko Hirschmüller is through shrinking global from a 2D problem to a 1D problem by limiting the search space from the entire overlap to samples along regularly spaced straight paths extending regularly in predefined directions through the overlaps

[21–23]. The shrinking idea appeared to be ingenious and feasible. This simplified global matching approach, called Semi-Global Matching (SGM), produce high quality results beyond expectations, and revolutionized and revitalized photogrammetry. From the year 2005 SGM became rapidly successful for a broad range of applications. Since it produces dense point clouds, SGM is often referred to as Dense Image Matching (DIM).

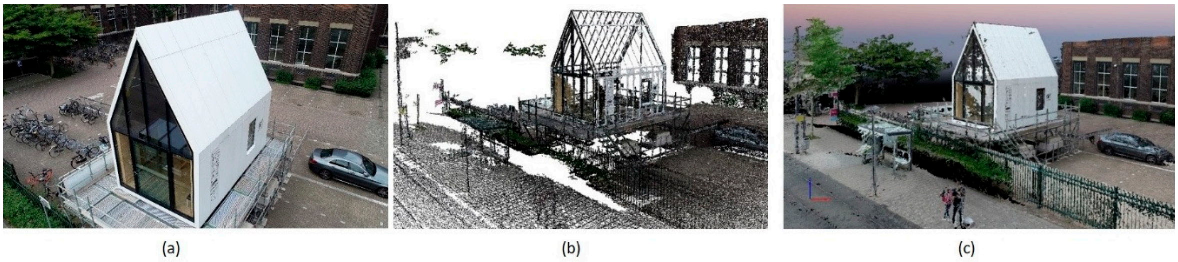

Figure 11. (a) Image captured from a UAS platform showing building with little texture, (b) Point cloud generated by the SIFT-based FBM approach, (c) Point cloud generated by SGM as implemented in Pix4Dmapper software (courtesy: Delft University of Technology, Netherlands).

SGM generates high point densities even for objects with little texture compared to the SIFT-based FBM approach (Figure 11). SGM has been extensively investigated for a variety of photogrammetric applications and image types including aerial images [24], terrestrial and extraterrestrial satellite data [25,26], and video sequences [27,28]. The potential of SGM for creating dense DEMs from aerial images has been convincingly demonstrated [28]. SGM shows a good balance between computational requisites, accuracy and detail and is thus well-suited for creating dense point clouds for many practical applications including the creation of DEMs and 3D city models. Each type of imagery and application will require tailor-made post-processing in order to get rid of imperfections in the end products and to increase quality. SGM has been implemented in a variety of photogrammetric software packages. In depth mathematical treatments are given in the above references. A treatment at entrance level is provided in [5] (pp. 96-102).

4. Products and Performance

This section presents two important standard end-products generated along modern photogrammetric workflows – digital elevation models (DEM) and orthomosaics – followed by methods to assess geometric accuracy using a DEM as example.

4.1. Products

4.1.1. Digital Elevation Model (DEM)

The basic output of a photogrammetric workflow is a 3D point cloud. Although photogrammetry is a crucial data source for many users from a wide spectrum of applications, the focus here will be on representations of the Earth surface obtained from airborne and spaceborne imagery. Here the point clouds represent topography, which are indispensable for analyzing flood threat, landslide risk and many other earth-related physical processes. Point clouds are also exploited for the generation of orthomosaïcs, regularly used as background in GIS applications, and 3D landscape and building/city models. DEM is an overarching term encompassing DSM, DTM and DTM+. Image matching produces a Digital Surface Model (DSM) – an umbrella surface including bare ground, buildings, foliage and other non-moving and moving objects. A DSM is usually not the end product since many applications require a next step. Cars and other moving objects have to be (semi)automatically filtered out. In applications including water drainage and forestry one wants a representation of the bare ground, which requires filtering out of buildings and all other above ground objects. This transformation requires the classification of the DSM in ground and non-ground points, called ground-filtering. A plethora of ground filtering methods have been developed,

Preprints.org (www.preprints.org) | NOT PEER-REVIEWED | Posted: 18 March 2026 doi:10.20944/preprints202603.1489.v1

although based on a few principles [5] (pp. 221-248). Ground filtering results in a Digital Terrain Model (DTM). Enriching a DTM with ridges, streams and other terrain features results in a DTM+. Draping orthomosaïcs over a DSM generates a 3D Digital Landscape Model (DLM), which is a virtual landscape suited for 3D mapping (Figure 12a). Enriched with the facades of buildings using oblique aerial images and ground based images captured from a car or human back, converts a DSM into a 3D building/city model (Figure 12b).


(a) (b)

Figure 12. (a) 3D Digital Landscape Model (DLM) of a quarry, i.e. a virtual landscape, generated by draping an orthoimage over a Digital Surface Model (DSM), created from images taken with a camera mounted on a UAS (source: [30]), (b) SGM point cloud of the Cathedral of Rostov-on-Don generated from UAS images (source: [5] (p. 102), courtesy: Racurs, Moscow, Russia).

4.1.2. Orthomosaics

An aerial orthoimage has undergone a transformation from perspective projection to a (quasi)orthogonal projection. Typically, a set of adjacent orthophotos is combined into a single orthomosaic. If the terrain may be considered flat, tilt correction, using GCPs, suffices. Relief-rich areas require a DEM for correcting relief distortions. Draping orthomosaics over a DEM produces a 3D DLM—a virtual landscape—that allows a surveyor to measure 3D coordinates of points of interest in the office. Since lean-over and occlusion increase with increasing distance from the image center both will be never absent in relief-riche areas. Using only the center parts of images taken with high along-track (e.g. 80%) and across-track (e.g. 60%) combined with a large focal length results in near-real orthogonal projections. The production of such true orthoimages requires many images and a dense DEM. Application examples are cultural heritage mapping (Figure 13a) and gravel quarry mining (Figure 13b).


(a) (b)

Figure 13. (a) Part of an orthomosaic of Rapa Nui created by UAS photogrammetry; statues' shadows point in different directions since the mosaic combines multiple images taken at different times (source: [31]), (b) Contour

lines superimposed on the orthomosaic of a basalt quarry in Ukraine generated from images taken with a consumer-grade camera mounted on a UAS (source: [32]).

4.2. Accuracy Assessment

When conducting experiments to test the suitability of a photogrammetric product for a particular task, the results must be compared with reference data. Also in practical surveys comparison is necessary to check whether the product meets the specification or standards. One of the most explored photogrammetric data products are (dense) 3D point clouds for which four evaluation measures are essential: Point Density, Homogeneity, Root Mean Square Error (RMSE) and Systematic Error (SE) – also called Mean Error (ME). Point density is the number of points detected by image matching in a region divided by the area of the region, usually expressed as points/m^2. Homogeneity refers to the extent to which points are well distributed over the object space and is expressed as the total area of gaps, e.g. due to absence of texture or presence of water bodies, divided by the area of the region. Here computation of RMSE and SE are shown for DEMs. A small subsample of the DEM elevations, which are well-distributed over the area, are compared with elevation reference values, measured with a precision, which is better (say ten times) than the DEM values and often measured with high definition DGNSS-receivers. RMSE is expressed as:

$$RMSE = \sqrt{\frac{\sum_{i=1}^{n}(Z_i - z_i)^2}{n}} \tag{14}$$

Z_i refers to the reference values, z_i to the corresponding DEM elevations and n is the number of points involved in the evaluation. SE is expressed as:

$$SE = \frac{\sum_{i=1}^{n}(Z_i - z_i)}{n} \tag{15}$$

If SE is zero, RMSE is essentially a standard deviation. This is based on the assumption that errors in the DEM are randomly and normally distributed. If SE is non-zero, RMSE will be biased, which violates the assumption that it may be a substitute for the standard deviation. A measure which resemblances better the standard deviation (σ) is to correct the DEM height for the systematic error by subtracting the SE from the DEM height and to divide by n-1 [33]:

$$\sigma = \sqrt{\frac{\sum_{i=1}^{n}(Z_i - SE - z_i)^2}{n-1}} \tag{16}$$

Since it will rarely occur that Z_i and z_i; i=1,...n, will be located at the same point in the horizontal plane, interpolation has to be conducted to warrant that both points do have the same planar coordinates. This step may introduce interpolation errors. Many interpolation methods are available in software. Refer to [5] (pp.193-220) for selection of proper interpolation methods and to [5] (pp. 242-245) for quality measures to assess the accuracy of the many available ground filtering methods.

5. Discussion

This article provides a concise introduction to the basics of modern photogrammetry. To deepen knowledge a variety of textbooks are available for consultation. A comprehensive treatment of all aspects of photogrammetry, including in depth mathematics, is provided by the fist thick Manual of Photogrammetry [7]. Introductions to the basics of (aerial) photogrammetry have been written by Mikhail et al. (2001); Kraus (2007); Wolf et al. (2013); Weilberg (2016), [34–36]. Schenk (1999) [1]; Egels & Kasser (2001) [2]; Mikhail et al. (2001) [3] have written early textbooks elaborating upon the principles of digital photogrammetry, while Linder (2018) [37] provides an introduction to digital photogrammetry aimed at serving practicians. Graham & Koh (2013) [38] focus on the surveying aspects of aerial digital photogrammetry. Atkinson (2003) [39] and Luhmann et al. (2014) [40] describe in detail the principles of extracting geoinformation from images taken from ground-based platforms

– close range photogrammetry. Gruen & Huang (2001) [41] brought together a volume dedicated to the calibration and orientation of cameras in computer vision, written by various photogrammetry and computer vision experts. Hartley & Zisserman (2004) [42] describe the geometric aspects of images from a computer vision perspective. Lemmens (2023) [5] covers in detail the fundamentals of digital photogrammetry, 3D computer vision and Lidar as technologies for point cloud collection, processing, and applications. Various books deal with a specific application field of photogrammetry. In this framework Dai & Lu (2011) [43] wrote a booklet on applying close-range digital photogrammetry in construction. The importance of DEMs in all geosciences and practices is reflected by textbooks on digital terrain representations and analysis, including: El-Sheimy et al. (2005); Li et al. (2005); Peckham & Jordan (2007); Florinsky (2016), [44–47]. The use of UAS as an appreciated platform for photogrammetric surveys has tremendously increased the last decade, accompanied by the release of specialized textbooks including those written by Armenakis & Patias (2019); Carvajal-Ramírez et al. (2021); Titchener (2024); Dowell (2025), [48–51].

Abbreviations

The following abbreviations are used in this manuscript:

CCD	Charge-coupled device
DEM	Digital Elevation Model
DLM	Digital Landscape Model
DoG	Difference-of-Gaussians
DSM	Digital Surface Model
DTM	Digital Terrain Model
DGNSS	Differential GNSS
FBM	Feature Based image Matching
FoV	Field of View
GCP	Ground Control Point
GIS	Geographical Information System
GNSS	Global Navigation Satellite System
GPU	Graphical Processing Unit
IMU	Inertial Measurement Unit
LoG	Laplacian of Gaussian
LSA	Least Squares Adjustment
LSM	Least Squares image Matching
Lidar	Light Detection And Ranging, also called laser scanning
ME	Mean Error
POS	Positioning and Orientation System
RMSE	Root Mean Square Error
SE	Systematic Error
SfM	Structure from Motion
SGM	Semi-Global Matching
SLAM	Simultaneous Localization And Mapping
UAS	Unmanned Airborne System
WGS84	World Geodetic System 1984

Appendix A

In an attempt to computationally simulate the human visual system Marr & Hildreth developed an operator for detecting abrupt grey value changes in digital images [52]. This operator, called Laplacian of Gaussian (LoG), is still widely used in computer vision applications, e.g. as part of the SIFT operator (subsection 3.2.3). As is the case with the Dreschler-Nagel interest operator this operator exploits second derivatives of the grey value function, but combines the derivatives differently. The second derivatives along the orthogonal row and column directions are added based on the Laplacian:

$$\Delta G(x,y) = \frac{\partial^2 G}{\partial x^2} + \frac{\partial^2 G}{\partial y^2} = G_{xx} + G_{yy} \tag{A1}$$

With G_{xx} and G_{yy} defined in Equation 9, resulting in the 3 x 3 discrete Laplacian kernel:

$$\Delta G = G * \begin{bmatrix} 0 & 1 & 0 \\ 1 & -4 & 1 \\ 0 & 1 & 0 \end{bmatrix} \tag{A2}$$

The response of second derivatives is sensitive to noise. The noise effect is reduced by combining the Laplacian with a Gaussian smoothing kernel, which is derived from the 2D Gaussian function:

$$G(x,y) = \frac{1}{2\pi\sigma^2} e^{-\frac{x^2+y^2}{2\sigma^2}} \tag{A3}$$

For example, when $\sigma = 0.8$ and the kernel size is set to 3 x 3, the kernel becomes:

$$\frac{1}{16}\begin{bmatrix} 1 & 2 & 1 \\ 2 & 4 & 2 \\ 1 & 2 & 1 \end{bmatrix} = \frac{1}{16}\begin{bmatrix} 1 \\ 2 \\ 1 \end{bmatrix} * \begin{bmatrix} 1 & 2 & 1 \end{bmatrix} \tag{A4}$$

Where $*$ denotes convolution. The LoG operator is computational expensive and therefore often replaced by the difference of two Gaussian smoothed versions of the same image. The one Gaussian kernel is smaller than the other kernel. This operation is called Difference-of-Gaussians (DoG). To further reduce computation time, the implementation of the Gaussian function can be done by first convolving the image with two 1D Gaussian functions in row and column direction, one after the other, as shown in the right side of equation A4. Instead of changing the LoG size, the size of the image is reduced by constructing an image pyramid with at its base the original, full-size image and at subsequent higher levels images generated from uniting n × n pixels, where n is e.g. 2. The Laplacian is isotropic, i.e. the response is independent of the orientation of edges and distinctive points with respect to the image grid. So, the output is insensitive to the orientation of the camera with respect to the scene.

References

1. Schenk, T. Digital photogrammetry: Background, Fundamentals, Automatic Orientation Procedures. Terra Science, Laurelville, OH, US, **1999**, Volume 1, 428 pages.
2. Egels, Y.; Kasser, M. Digital photogrammetry. Taylor & Francis Ltd, ISBN 978-0748409457, **2001**, 376 pages.
3. Mikhail, E.M.; Bethel, J.S.; McGlone, J.C. Introduction to modern photogrammetry. Wiley, New York, Chichester, US, **2001**, 496 pages.
4. Lemmens, M.; Lemmen, C.; Wubbe, M. Pictometry: potentials for land administration. 6th FIG regional conference, San José, Costa Rica, **2007**.
5. Lemmens, M. Introduction to Pointcloudmetry – Point Clouds from Laser Scanning and Photogrammetry. Whittles Publishing, Dunbeath, Caithness, Scotland, UK, ISBN: 978-1-84995-479-2, portopress.com/products/9781849954792_introduction-to-pointcloudmetry, **2023**, 349 pages.
6. Fraser, C.S. Digital camera self-calibration. ISPRS Journal of Photogrammetry & Remote Sensing, 52(4), **1997**, pp. 149-159.
7. Manual of Photogrammetry, 6th edition. Editor: McGlone, J.C., American Society for Photogrammetry and Remote Sensing, **2013**, 1318 pages.
8. Lemmens, M.J.P.M. A survey on stereo matching techniques. International Archives of Photogrammetry and Remote Sensing, Volume 27, no. B8, **1988**, pp. 11-23.
9. Ackermann, F. High precision digital image correlation. Proceedings 39th photogrammetric week, Institut für Photogrammetrie, Stuttgart, Germany, Heft 9, **1983**, pp. 231–243.
10. Ackermann, F. Digital Image Correlation: Performance and Potential Application in Photogrammetry. Photogrammetric Record, 11(64), **1984**, pp. 429-43.

11. Gruen, A.W. Adaptive Least Squares Correlation: A powerful image matching technique. S. Afr. Journal of Photogrammetry, Remote Sensing and Cartography, 14(3), **1985**, pp. 175-187.
12. Lowe, D.G. Object recognition from local scale-invariant features. International Conference on Computer Vision, Corfu, Greece, **1999**, pp. 1150-1157.
13. Lowe, D.G. Distinctive image features from scale-invariant keypoints. International Journal of Computer Vision, 60(2), **2004**, pp. 91-110.
14. Förstner, W. A Feature Based Correspondence Algorithm for Image Matching. Int. Arch. of Photo gr. vol. 26-III, Rovaniemi, Finland, **1986**, pp. 1-17.
15. Förstner, W.; Gulch, E. A Fast Operator for Detection and Precise Location of Distinct Points, Corners and Centres of Circular Features. Proc. ISPRS Intercomm. Conf. on fast processing of photogrammetric data, Interlaken, Switzerland, **1987**, pp. 281-305.
16. Harris, C.; Stephens, M. A combined corner and edge detector. Proc. of the Alvey Vision Conference, **1988**, pp. 147 – 151.
17. Dreschler, L.; Nagel, H.-H. Volumetric model and 3D trajectory of a moving car derived from monocular TV frame sequences of a street scene. Computer Graphics and Image Processing, Volume 20, **1982**, pp. 199-228.
18. Dreschler, L.S.; Nagel, H.-H. On the Selection of Critical Points and Local Curvature Extrema of Region Boundaries for Interframe Matching. In: Huang T.S., Eds.; Image Sequence Processing and Dynamic Scene Analysis. NATO ASI Series (Series F: Computer and System Sciences), Springer, Berlin, Heidelberg, **1983**, Volume 2, pp. 542-544.
19. Miksik, O.; Mikolajczyk, K. Evaluation of local detectors and descriptors for fast feature matching. 21st Intern. Conf. on Pattern Recognition, Tsukuba, Japan, **2012**, pp. 2681- 2684.
20. Bay, H.; Ess, A.; Tuytelaars, T.; Van Gool, L. Speeded-up robust features (SURF). Computer Vision and Image Understanding, **2008**, Volume 110 (3), pp. 346–359.
21. Hirschmüller, H. Accurate and Efficient Stereo Processing by Semi-Global Matching and Mutual Information. IEEE Conference on Computer Vision and Pattern Recognition, **2005**, Volume 2, pp. 807-814.
22. Hirschmüller, H. Stereo processing by semiglobal matching and mutual information. IEEE Transactions on Pattern Analysis and Machine Intelligence, **2008**, Volume 30 (2), pp. 328–341.
23. Hirschmüller, H. Semi-Global Matching – Motivation, Developments and Applications. Photogrammetric Week, Edt. Dieter Fritsch, Wichmann/VDE Verlag, Belin & Offenbach, Germany, **2011**, pp. 173-184.
24. Hirschmüller, H.; Scholten, F.; Hirzinger, G. Stereo vision based reconstruction of huge urban areas from an airborne pushbroom camera (HRSC). In: Lecture Notes in Computer Science: Pattern Recognition, Proceedings of the 27th DAGM Symposium, Springer, **2005**, Volume 3663, pp. 58–66.
25. Krauss, T.; Lehner, M.; Reinartz, P. Generation of coarse 3D models of urban areas from high resolution stereo satellite images. Int. Archives of the Photogrammetry and Remote Sensing, **2008**, Volume XXXVII. Part B1, pp. 1091-1098.
26. Alobeid, A.; Jacobsen, K.; Heipke, C. Comparison of Matching Algorithms for DSM Generation in Urban Areas from Ikonos Imagery. Photogrammetric Engineering & Remote Sensing, **2010**, Volume 76 (9), pp. 1041–1050.
27. Heinrichs, M.; Rohdehorst, V.; Hellwich, O. Efficient Semi-Global Matching for Trinocular Stereo. International Archives of the Photogrammetry, Remote Sensing and Spatial Information Sciences, Munich, Germany, **2007**, Volume XXXVI, Part 3/W49A, pp. 185-190.
28. Gerke, M. Dense Image Matching in Airborne Video Sequences. Int. Archives of the Photogrammetry, Remote Sensing and Spatial Information Sciences, Beijing, China, **2008**, Volume XXXVII, Part B3b, pp. 639-644.
29. Rothermel, M.; Haala, N. Potential of dense image matching for the generation of high quality digital elevation models. Int. Archives of the Photogrammetry, Remote Sensing and Spatial Information Sciences, **2011**, Volume XXXVIII-4/W19, pp. 271-276.
30. Op ‘t Eyndt, T.; Volkmann, W. UAS as a Tool for Surveyors – Virtual Surveying instead of Tripods and Trucks. GIM International UAS Special, **2013**, pp. 26-29.

31. Norambuena, P.; Sainz, J. UAS Survey of Rapa Nui - Capturing the World's Most Remote Inhabited Island, GIM International, **2016**, Volume 30(6), pp. 17-19.
32. Gorkovchuk, D.; Gorkovchuk, J.; Hutnyk, B. Low-cost UAS Photogrammetry for Mining – Exploring Consumer-grade Copters for Quarry Mapping, GIM International, **2017**, Volume 31(11), pp. 20-23.
33. Fisher, P.F.; Tate, N.J. Causes and Consequences of Error in Digital Elevation Models. Progress in Physical Geography, **2006**, Volume 30, pp. 467-489.
34. Kraus, K. Photogrammetry: Geometry from Images and Laser Scans, 2nd edition. Walter de Gruyter, Germany, **2007**, 474 pages.
35. Wolf, P.R.; Dewitt, B.A.; Wilkinson, B.E. Elements of photogrammetry with applications in GIS. 4th edition, McGraw-Hill Professional, **2013**, 640 pages.
36. Weilberg, M. (Ed.) Photogrammetry and remote sensing. Syrawood Publishing House, ISBN 978-1682861073, **2016**, 216 pages.
37. Linder, W. Digital photogrammetry: a practical course. 4th edition, Springer, **2018**, 232 pages.
38. Graham, R.; Koh, A. Digital Aerial Survey: Theory and Practice. Whittles Publishing, Dunbeath, Caithness, Scotland, UK, **2013**, 272 pages.
39. Atkinson, K.B. (Ed.) Close range photogrammetry and machine vision. Whittless Publishing, Dunbeath, Caithness, Scotland, UK, **2003**, 384 pages.
40. Luhmann T.; Robson S.; Kyle, S.; Boehm, J. Close-range photogrammetry and 3D imaging, 3th edition. Walter de Gruyter, Germany, ISBN: 978-3110607246, **2019**, 858 pages.
41. Gruen, A.; Huang, Th.S. (Eds.) Calibration and orientation of cameras in computer vision. Springer Series in Information Sciences, vol. 34, Springer Berlin, Heidelberg, Germany, **2001**, 236 pages.
42. Hartley, R.; Zisserman, A. Multiple View Geometry in Computer Vision. 2nd Edition, Cambridge University Press, **2004**, 670 pages.
43. Dai, F.; Lu, M. Applied close-range photogrammetry in construction for 3D modeling, quantity surveying, and augmented reality. LAP Lambert Academic Publishing, ISBN 978-3844322866, **2011**, 112 pages.
44. El-Sheimy, N.; Valeo, C.; Habib, A. Digital Terrain Modeling: Acquisition, Manipulation And Applications. Artech House, **2005**, 257 pages.
45. Li, Z.; Zu, Ch.; Gold Ch. Digital Terrain Modeling - Principles and Methodology. CRC Press, USA, **2004**, 323 pages.
46. Peckham, R.J.; Jordan, G. (Eds.) Digital Terrain Modelling: Development and Applications in a Policy Support Environment. Lecture notes in Geoinformation and Cartography, Springer Berlin, Heidelberg, New York, **2007**, 310 pages.
47. Florinsky, I. Digital Terrain Analysis in Soil Science and Geology. 3rd Edition, Academic Press, **2025**, 486 pages.
48. Armenakis, C.; Patias, P. (Eds.) Unmanned vehicle systems for geomatics: towards robotic mapping. Whittles Publishing, Caithness, Scotland, UK, **2019**, 335 pages.
49. Carvajal-Ramírez, F.; Agüera-Vega, F.; Martínez-Carricondo, P. (Eds.) UAV Photogrammetry and Remote Sensing; printed edition of the special issue published in Remote Sensing, MDPI AG, **2021**, 258 pages.
50. Titchener, I.P. A brief introduction to drone mapping, surveying and photogrammetry, Independently Published, ISBN 979-8338284674, **2024**, 112 pages.
51. Dowell, Th. The fundamentals of drone photogrammetry, mapping, and survey. Drones Inbound, ISBN 979-8998582912, **2025**, 229 pages.
52. Marr, D.; Hildreth, E. Theory of Edge detection. Proc. R. Soc. Lond., **1980**, Volume B 207, pp. 187-217.